JOURNAL OF MATERIALS SCIENCE **40** (2005) 4231 – 4238

Metal injection molding of shape memory alloys using prealloyed NiTi powders

E. SCHÜLLER, L. KRONE, M. BRAM, H. P. BUCHKREMER, D. STÖVER
Forschungszentrum Juelich, IWV1, 52428 Juelich, Germany
E-mail: l.krone@fz-juelich.de

Metal injection molding (MIM) was applied for the production of shape memory parts using prealloyed NiTi powders with different Ni contents as starting materials. The MIM process allows the production of near-net-shape components without the occurrence of rapid tool wear as found in the case of conventional machining operations. With optimized manufacturing conditions, including feedstock preparation, injection parameters and sintering conditions, densities of more than 98% of the theoretical value could be achieved. Determination of the phase transformation behavior, as a basic requirement for the shape memory effect, was done by differential scanning calorimetry (DSC). In a first approach, tensile tests in the austenitic state showed pseudoelastic behavior. An elongation at failure of 3.8% was found. For martensite, up to 5% was obtained. Reasons for the lower strain compared to melted NiTi alloys are discussed. For martensitic samples the one-way shape memory effect (1WE) was demonstrated.

1. Introduction

With their outstanding mechanical properties NiTi shape memory alloys (SMAs) are of great industrial interest as actuators and also for biomedical applications [1–3]. Shape memory behavior is based on a diffusionless and reversible phase transformation between the low-temperature martensite and the high-temperature austenite phase. The transformation is characterized by the phase transformation temperatures (PTTs) with a start, a peak and a finish temperature (abbreviations M_s, M_p and M_f for the martensite, A_s, A_p and A_f for the austenite), which can be determined for example by differential scanning calorimetry (DSC). Under certain conditions, the transformation is more complex with the intermediate R-phase mainly occurring during the cooling cycle (multi-step transformation) [4, 5]. For technical applications, two kinds of shape memory effects are preferentially used. The "one-way effect" is exploited for coupling elements and medical implants (e.g. staples for foot surgery or stents). After a deformation in the martensitic state, parts stay deformed until they are heated above A_f then returning to their original shape. The "pseudoelastic" or "superelastic" behavior is based on the formation of stress-induced martensite (SIM) in a temperature range between A_f and a temperature M_d, which is the limit temperature for SIM formation. The pseudoelasticity is characterized by a large increase of strain without or with only a small increase in stress (pseudoelastic plateau). Plateau strains of about 8% are observed in melted alloys.

The control and adjustment of PTT is one of the main requirements for commercial use of SMA. For NiTi alloys these temperatures are sensitive to Ni content changes in the NiTi matrix phase [6]. This content is influenced by several factors such as the occurrence of precipitates and additional stable but non-transforming phases, e. g. oxides caused by the impurity content [7–10]. Apart from that the enhancement of brittleness due to the oxide phases decreases the mechanical properties [11]. Therefore impurities have to be kept at a low level. Commercially available NiTi components are commonly produced by arc or induction melting. Hot working steps have to be performed to improve the microstructure. By cutting, drawing, drilling etc. the parts receive their final dimensions although the wear of cutting tools is high for NiTi alloys [12] and the materials loss is always a factor of cost.

To overcome the problems of melting and subsequent machining, alternative production routes are being developed for NiTi. In this context, powder metallurgical (PM) methods are of increasing interest. For semi-finished NiTi parts with high density, hot isostatic pressing (HIP) is a promising route for both elemental powder mixtures and prealloyed powders [13–15]. But to reduce the costs for the cutting tools and materials loss near-net-shape techniques are required such as metal injection molding (MIM), a combination of polymer injection molding and powder metallurgy. Metal powder of a suitable size and shape is mixed with an organic (polymeric) binder or binder mixture to obtain a feedstock. As it is a source of increased impurity content in the finished parts, the amount of binder has to be kept as low as possible. But it has to be high enough to ensure a good feedstock flowability during the injection process. Injection molding devices are used to form green bodies. The as-molded

TABLE I Some characteristic values for the starting powders

Powder	Ni content (At%)	Particle Size, (μm) d_{10}	d_{50}	d_{90}	Oxygen (wt%)	Nitrogen (wt%)	Carbon (wt%)	Phase transformation temperatures (°C) A_s	A_m	A_f	M_s	M_m	M_f
A	50.9	8	18	37	0.14	0.0044	0.08	−48	−5	14	−0.4	−78	—
B	49.5	7	17	37	0.12	0.002	0.08	51	63	77	40	27	14

components are usually debinded in two steps. First, an open porosity is achieved by either solvent extraction, or catalytic or thermal capillary-force-assisted debinding. In a second step, binder is burnt out through the occurring porosity. At least, the debinded parts are sintered to nearly full density. The MIM process becomes economical if large quantities of complex shaped parts are required. For alloys such as ferrous metals detailed descriptions of every processing step can be found in the literature [16]. But up to now little is known about MIM of NiTi alloys [17–19]. For elemental powder mixtures of Ni and Ti an anisotropic swelling of compounds during sintering is well known [20]. Therefore, Bram *et al*. [15] conducted MIM experiments with prealloyed powder. The influence of the polymeric content of the feedstock on the die filling behavior is shown and some results for sinterability, impurity level and transformation temperatures are given.

The present investigation is based on the abovementioned work. Examinations were focused on the dependence of properties on the sintering conditions (temperature and atmosphere). Microstructure, density and phase formation are determined. The phase transformation temperatures are investigated using the DSC method. With sintering parameters found to be best for the given feedstock, tensile test samples were prepared. Characterization of the mechanical properties and the shape memory behavior is given. The occurrence of pseudoelasticity and one-way effect is shown on a macroscopic scale.

2. Experimental

Two prealloyed NiTi powders prepared by gas atomization (Nanoval, Germany) were used. The Ni content given by the manufacturer is 50.9 at.% for powder "A" and 49.5 at.% for powder "B". In Table I, the characteristic properties of both powders are given. Particle size and impurity content are quite similar for powders A and B. Feedstocks were prepared by mixing each powder with a sufficient amount of two-component binder consisting of a polyamide wax and a polyethylene (both Clariant, Germany). The volumetric ratio of wax to polymer was 60:40. Homogenization was done in a heatable kneader at about 150°C for 2 h.

Two different molds were used for the present investigation: one for flat bar tension specimens and one for hollow cylinders of 30 mm in length and 2 mm wall thickness (Fig. 1). Injection molding was performed on a 270 CMD, 400–140 device (Aarburg, Germany). Molding parameters such as die and nozzle temperature have to be adjusted for each die and feedstock. Table II gives the preferred parameter set.

Green bodies were dewaxed at temperatures up to 180°C by a process called "wicking" using the capillary force of an Al_2O_3 granulate bed. A thermal debinding step at 480°C followed. For powder A, a sintering study was performed at 1100, 1200 and 1270°C in vacuum and argon flow atmosphere. Shrinkage determination and evaluation of the dimensional accuracy were done on the cylinders. For powder B, sintering conditions found to be best for powder A did not lead to sufficient density and a reaction with the sintering support occurred. Therefore, the sintering temperature was decreased from 1270 to 1250°C. To balance the reduced temperature, the dwell time was extended from 5 to 10 h. Investigation of phase transformation temperatures by differential scanning calorimetry (DSC) and determination of impurity content of oxygen, nitrogen and carbon were done on chips or small parts machined from the compacts. For powder A, which is able to form Ni_4Ti_3 precipitates due to its Ni content >50.5 at%, the specimens were heat-treated in evacuated quartz glass capsules. Solution treatment was done at 850°C, 1 h followed by an annealing step at 500°C for 1 h to achieve comparable precipitation states in all samples. Each treatment was followed by water quenching. DSC measurements were performed in a temperature range between −120°C and +150°C with a heating and cooling rate of 10 K/min (2920 MDSC, TA Instruments).

Specimens were prepared for metallographic investigations. The apparent phase composition after sintering and changes in phase formation as a function of heat treatment steps was analyzed by XRD (Diffractometer, D500, Siemens). Energy-dispersive X-ray analysis (EDX) in combination with scanning electron microscopy (1530-Gemini, LEO) was done. Tensile test specimens were prepared from both powder feedstocks. For powder A samples, the same heat-treatment was

TABLE II Optimized parameters for the injection molding

Parameter	Values
Nozzle temperature	145°C
Mold temperature	50°C
Injection pressure	700 bar
Mass flow	30 ccm/s

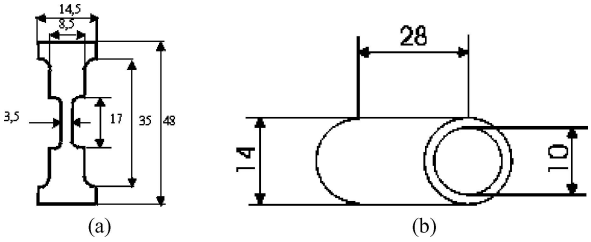

Figure 1 Sample geometry (a) tensile test specimen, (b) hollow cylinder.

TABLE III Impurity content and phase transformation temperatures. All A-powder samples were heat treated (850°C. 1 h + 500°C. 1 h). For powder B sample, the R-phase temperatures are estimated from the printout of the DSC curve

	Sintering conditions			Impurity content (wt%)			Phase transformation temperatures (°C)								
Powder	Atmosphere	Temp.	Time (h)	O	C	N	R_s	R_p	R_f	M_s	M_p	M_f	A_s	A_p	A_f
A	Vacuum	1100°C	5	0.3524	0.112	0.0042	21	7	−2	−55	−68	−88	−5	6	19
A		1200°C	5	0.339	0.156	0.0104	23	10	1	−69	−87		−4	4	10
A		1270°C	5	0.3013	0.087	0.001	23	11	−1				−8	0	29
A	Ar-flow	1100°C	5	0.3525	0.114	0.0028	21	6	−2	−57	−78		−7	1	21
A		1200°C	5	0.3491	0.119	0.0096	14	6	−1	−26	−35	−53	3	14	20
A		1270°C	5	0.3135	0.112	0.0063	23	10	1	−25	−32	−44	−1	7	23
B	Vacuum	1250°C	10	0.0356	0.118	0.0053	55	26	0	−37	−55	−69	13	28	68

performed on tensile test specimens as for the chips. To achieve a defined surface quality, all samples were ground with emery paper of grade 1200. Mechanical testing was done with a Zwick-type 1387 electromechanical equipment at a strain rate of 0.5 mm min^{-1} in tension. To determine the pseudoelastic effect, which is based on the stress-induced transformation from austenite to martensite, a higher test temperature for powder A specimens was chosen than the austenite finish temperature A_f taken from the DSC examination. Test temperatures of 25°C (martensite/austenite mixed state) and 70°C (pure austenite) were chosen for powder B specimens to examine the influence of the different transformation states on the mechanical behavior. Pseudoplasticity is demonstrated by unloading tensile test specimens at 50°C, mainly in the austenitic state. To demonstrate the one-way effect, powder B samples were cooled down below −50°C using ice spray, deformed in the martensitic state using a three-point bending test, unloaded and then heated to temperatures higher than A_f.

3. Results

Fig. 2 shows the powder B tensile test geometry at different process states (as MIMed, partly debinded and sintered) and gives an impression of the shrinkage. Depending on the component contour, a shrinkage in the range of 8 to 13% is observed. This shrinkage has to be considered to end up with the required end geometry. Though there is a change in size, good dimensional accuracy is achieved by the MIM process. For fifteen tensile samples, length shrinkage was measured as 8.2 ± 0.2% (44.0 ± 0.1 mm). For the gauge width, 12.5 ± 0.8% (3.10 ± 0.05 mm) was determined. The average dimensional change of two powder A tubes was 9.5 ± 0.9% (25.29 ± 0.25 mm) in the longitudinal direction. For the wall thickness of the tubes an average shrinkage of 12.8 ± 0.2% (1.81 ± 0.05 mm) was determined. A slight distortion of the samples was found caused by the high sintering temperatures.

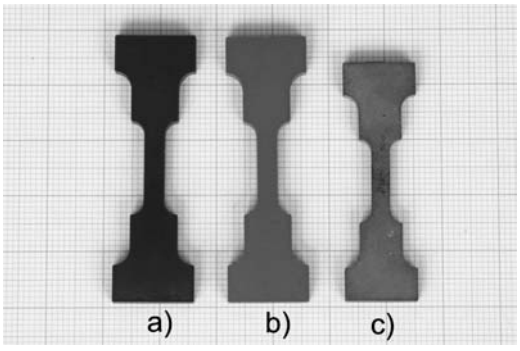

Figure 2 Powder B tensile test samples (a) as MIMed, (b) partly dewaxed, (c) sintered 1250°C, 10 h in vacuum.

3.1. Chemical analysis—impurity level

Oxygen, nitrogen and carbon contents were analyzed for MIM samples made of powder A on heat-treated chips and for powder B on small pieces without heat treatment. All results are given in Table III. The impurity level increases for all samples compared to the starting powder as a consequence of residuals from the binder. For powder A samples, the increase is unaffected by the sintering condition. An oxygen content of about 0.3 wt% was found for both powders.

3.2. Phase formation

Fig. 3a shows the microstructure of powder A samples after sintering. Three different gray scales are obvious. For the medium gray matrix phase, EDX analyses of the composition corresponds well to NiTi. The needle-like structure which disappears when heated indicates the martensite. For the dark gray phase, about 34 at% Ni is detected suggesting that it is $NiTi_2$. From the Ni : Ti ratio, $Ni_2Ti_4O_x$ is also a possible composition. Honma [10] and Olier [11] confirm that almost all contaminating oxygen precipitates in these types of oxides are due to the low solubility of oxygen in NiTi. The analysis of the black phase gives a Ti content of more than 90% so that it is assumed to be TiC. A large amount of organic binder is required to carry out the MIM process so carbide phases are estimated to be residuals from these components. During solution treatment, the formation of a double layer is observed at the surface (Fig. 3b). EDX analysis of the outer layer give a Ni to Ti ratio of about 1:2. Increased oxygen content is also detected for the thin layer so it is very likely that $Ni_2Ti_4O_x$ is formed on the surface. The formation of a Ti-rich oxide causes a Ti depletion below the layer. Determination by EDX shows a Ni content of 73 at% in this depletion zone. The Ni-rich Ni_3Ti phase occurs with less than 1 μm in thickness. Investigations from several research groups [21–23] confirm the double layer formation at increased

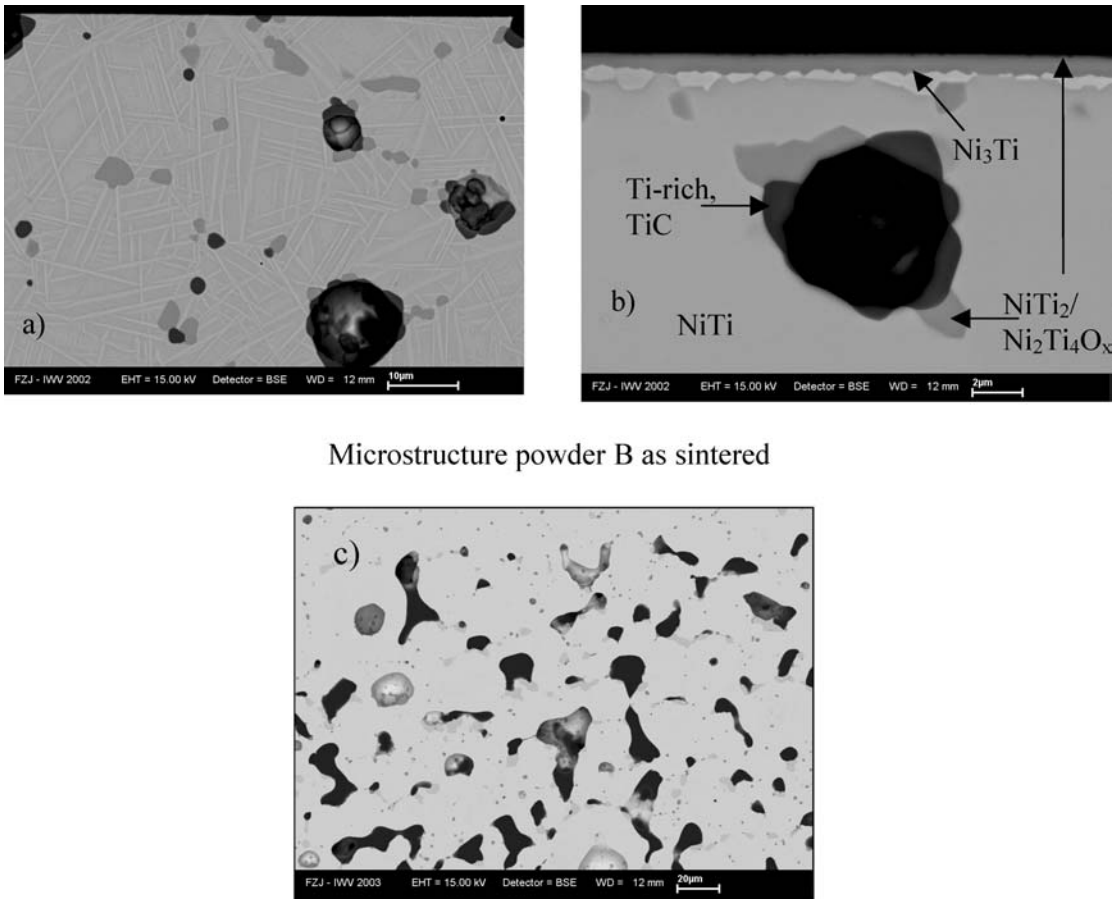

Figure 3 Microstructure of (a) powder A, as sintered 1270°C, 5 h in Ar-flow, (b) powder A, sintered and solution-treated 850°C, 1 h (layer formation at the surface is obvious), (c) powder B, as sintered 1250°C, 10 h in vacuum.

temperatures for NiTi alloys if oxygen is available in the surrounding atmosphere. The existence of the double layer is explained by the different affinity of Ni and Ti to oxygen causing the Ni and Ti ions to diffuse in opposite directions. The layer formation on the specimens' surface indicates an insufficient atmosphere in the quartz glass capsules used for heat treatment. Therefore, improvement of the heat treatment techniques and also the removal of the surface layers by electropolishing is considered for further investigation. In contrast to the oxygen-rich phase formed during heat treatment on the surface, the appearance of $NiTi_2$ or $Ni_2Ti_4O_x$ at the grain boundaries of the bulk material even after sintering can be explained by residuals of the organic feedstock components in combination with a thin oxide layer on the starting powder particles. For powder B samples the same microstructure is observed (Fig. 3c).

The phase composition of the samples was verified by XRD (Fig. 4). In addition, the XRD pattern for the starting materials is shown. For the starting powder A, single-phase NiTi is observed. Although on the basis of the composition with more than 50.5 at% Ni the metastable precipitation of Ni_4Ti_3 is also possible, the fast cooling during the gas atomization process hinders its formation. After sintering the MIM samples were furnace cooled. In this case, the conditions for precipitation are given and the metastable phase is formed in addition to the main NiTi phase. Further phases are obvious, but the overlap of $NiTi_2$ and $Ni_2Ti_4O_x$ peaks hinders a clear distinction [24]. With solution treatment and annealing, the $NiTi_2$ ($Ni_2Ti_4O_x$) peaks increase and Ni_3Ti occurs as a new phase. As expected, a decreased intensity of Ni_4Ti_3 peaks was found for the solution-treated sample. Phase composition and impurity level for samples sintered in vacuum are the same as that shown for sintering under argon flow (Table III).

Since powder A shows only austenite NiTi peaks, for powder B austenite and martensite coexist (Fig. 4b). By heating the powder up to 100°C (higher than A_f), martensite peaks disappear and the existence of detectable quantities of second phases in XRD can be excluded. After sintering at 1250°C for 10 h in vacuum, NiTi and $NiTi_2$/$Ni_2Ti_4O_x$ are found in the MIMed parts. The broadening of the NiTi main peak can be interpreted as the beginning of Ni_4Ti_3 formation, but with a weak crystallization state. A possible explanation is primarily the formation of Ti-consuming phases, which is coupled with an enhanced Ni content in the NiTi matrix. Obviously, the critical value of 50.5 at% Ni is exceeded and the formation of Ni-rich precipitates of Ni_4Ti_3 becomes possible.

3.3. Phase transformation temperatures—DSC

As expected from the Ni content, the starting powders show significant differences in the phase transformation temperatures (PTT) (Fig. 5a).

For the Ni-rich starting powder A, a flat peak is detected during cooling with a start temperature of

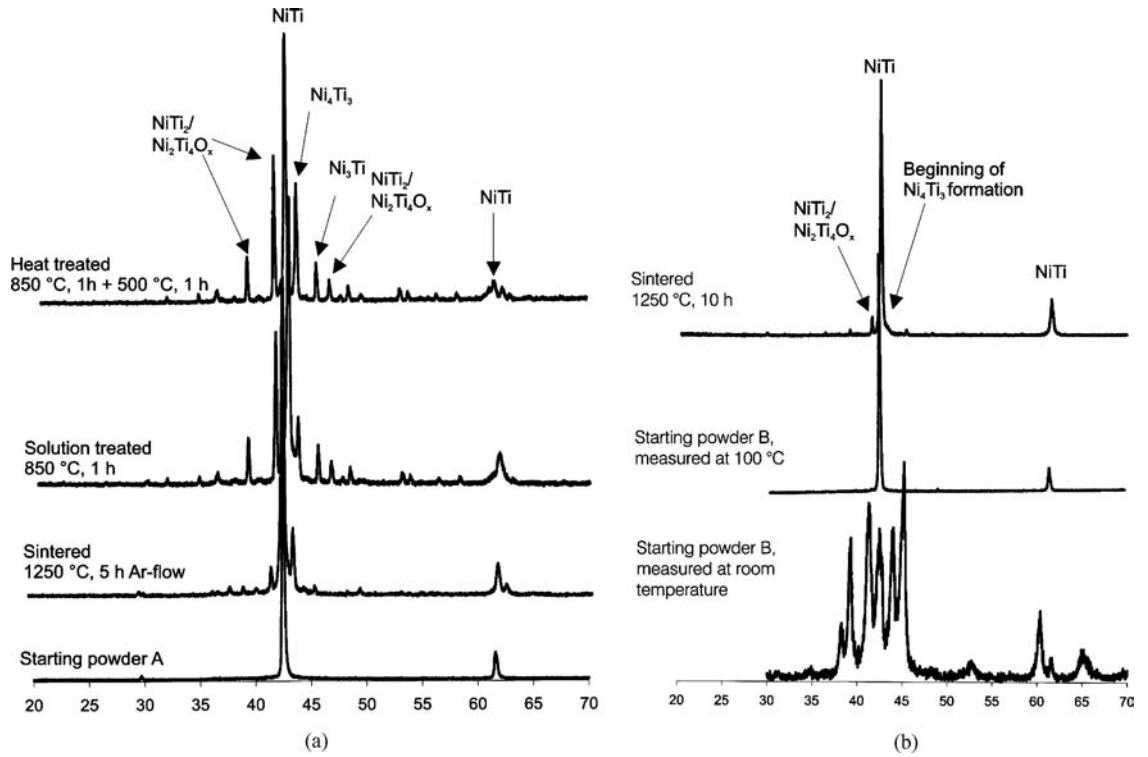

Figure 4 XRD pattern of (a) powder A samples and (b) powder B samples. For the starting powder B, pattern for room temperature shows martensite and austenite peaks. By heating the powder to 100°C, the transformation to austenite is obvious. No second phases are detected.

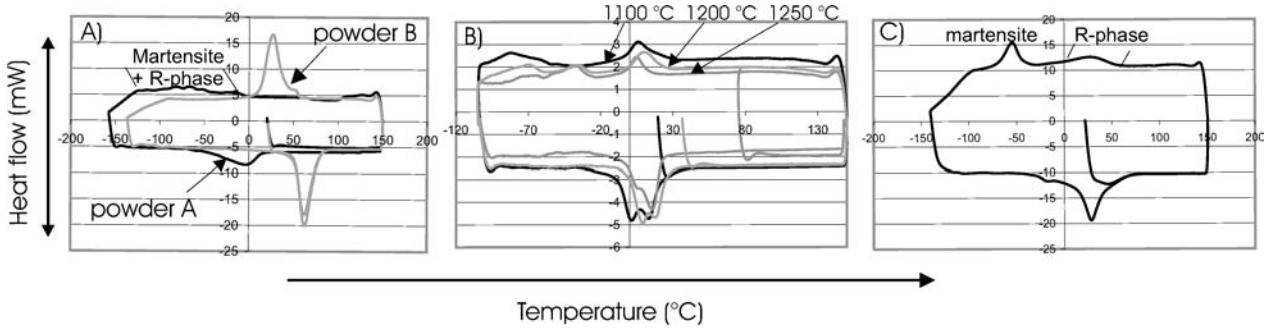

Figure 5 DSC curves for (a) starting powder A and B, (b) powder A samples sintered at different temperatures for 5 h in Ar-flow with heat treatment (830°C 1 h + 500°C, 1 h) and (c) powder B sample sintered at 1250°C, 10 h in vacuum without heat treatment.

about 0°C and a finish temperature below the measuring range (<−120°C). Peak temperature is estimated to be −78°C. The peak is identified as martensite. A separate clear *R*-phase peak was not detected. Therefore, from the width of the peak an overlap of martensite and *R*-phase is also possible. Since the martensite transformation temperature is directly correlated with the Ni content of the NiTi phase [6] and since the powder XRD shows only an austenite phase (Fig. 5a), the less pronounced peak is considered to be an indication of a non-uniform Ni distribution within the starting powder. Particles with a low amount of Ni will transform at higher temperatures than particles with a higher amount of Ni so that the overall transformation takes place in a wide temperature range. For alloys with less than 50 at% Ni, such as powder B, the M_s temperature is almost unaffected by the Ni:Ti ratio [6]. Therefore, even if a variation of the Ni content within the particles of powder B appears, it would not lead to a broad range of transformation temperatures. As a result, a distinct martensite peak is observed with a martensite start temperature at about 40°C.

From Table III it can be seen that with increasing sintering temperatures, the martensite transformation shifts to lower temperatures for powder A samples sintered in vacuum. For the 1200°C sample, the martensite finish temperature M_f is below −150°C. For the 1270°C sample the complete martensite transformation probably takes place at temperatures <−150°C and has therefore not been detected. *R*-phase and austenite transformation are almost unaffected by the sintering temperature. The hysteresis between the peak temperatures of these two phases is 2 to 10 K.

DSC curves for heat-treated powder A specimens sintered in Ar-flow are given in Fig. 5b. After sintering, a clear distinction between the *R*-phase and martensite transformation is obvious. While the *R*-phase is again almost unaffected by the sintering temperature, a shift of M_s from −50 to −25°C was found with increasing sintering temperatures. The transformation

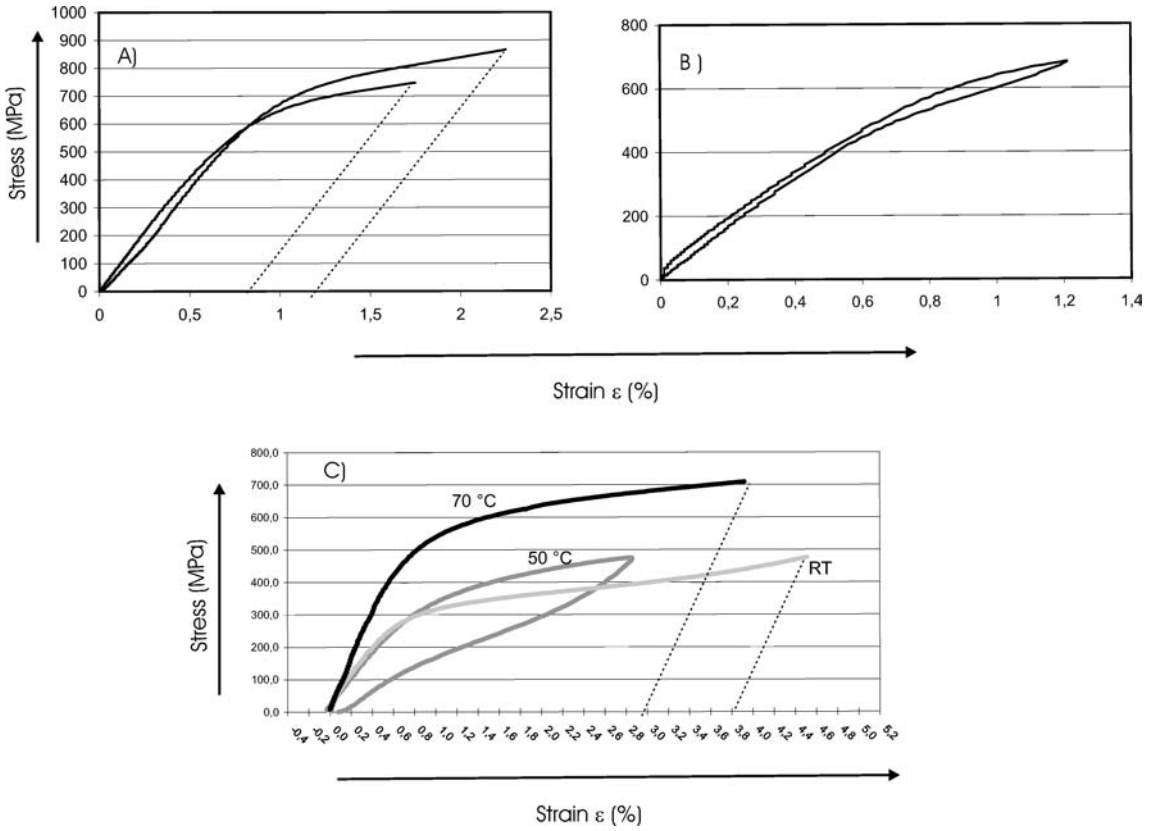

Figure 6 Stress-strain curves of (A) and (B) powder A specimens, sintered at 1270°C, 5 h in Ar-flow, measured at 40°C, (C) powder B specimens sintered at 1250°C, 10 h in vacuum, measured at different temperatures.

enthalpy of martensite and *R*-phase together was approximately 5 J/g, nearly the same as found for the transformation enthalpy determined from the broad flat cooling peak of the starting material. The enthalpy for the martensite to austenite transformation is given as 8 to 10 J/K, decreasing with increasing sintering temperatures. Compared to cast alloys, the transformation enthalpy is low. The appearance of the *R*-phase is an additional indication for the Ni_4Ti_3 precipitates, which were already detected by XRD [25, 26]. These precipitates deform the matrix or parent phase and induce stress fields where the *R*-phase is easily formed as an intermediate phase before the martensite phase occurs at much lower temperatures. Since precipitation formation is mainly influenced not by the sintering but by the post-sintering treatments, which are the same for all samples, the *R*-phase transformation is independent of the sintering conditions. In conclusion, no distinct correlation between sintering temperatures, impurity level and transformation behavior can be observed. The decrease of transformation temperature of 90 K with 1 at% oxygen as given by Shugo *et al*. [9] cannot be determined for the investigated samples, even for the high contents.

The DSC curve of a powder B sample sintered at 1250°C for 10 h in vacuum without additional heat treatment is given in Fig. 5c. An *R*-phase transformation, often associated with the existence of the metastable Ni_4Ti_3 phase detected by XRD, is obvious in the DSC curve. A_s is given as 13°C and A_f as 68°C. The martensite to austenite transformation is not therefore complete at room temperature and a mixture of both phases will exist. The martensite start temperature is given as −37°C.

3.4. Mechanical properties—Tensile tests

In the ideal case, stress-strain curves for austenite shape-memory alloys can be divided into four sections. Starting with the elastic deformation of the austenite, the pseudoelastic plateau occurs where stress-induced martensite is formed and $d\sigma/d\varepsilon$ is (nearly) zero. After a second region of elastic strain, the plastic deformation of the martensite follows up to final fracture. For the proof of pseudoelastic behavior based on the stress-induced formation of martensite, tensile tests were performed on powder A specimens at 40°C, according to the measured A_f of 25°C. The specimens are in the austenitic state.

The tensile test curves for two specimens prepared under the same conditions are given in Fig. 6A. A non-ideal behavior is observed. Up to a strain of 0.7%, the curve is linear reaching a stress value of about 550 MPa. With a further increase of strain, the slope of the curve decreases. Fracture occurs at a maximum strain of 1.7 and 2.2%, respectively, with a stress of 747 and 865 MPa. Fracture strain is measured as 0.8 and 1.15%. This strain is low compared to cast samples but it is in the same range as measured for the first samples prepared by hot isostatic pressing [27]. For HIP specimens, our latest investigations show that an improvement of the microstructure by reducing the amount of second phases leads to higher fracture strain (up to 7%, unpublished results). Therefore, further attempts to optimize

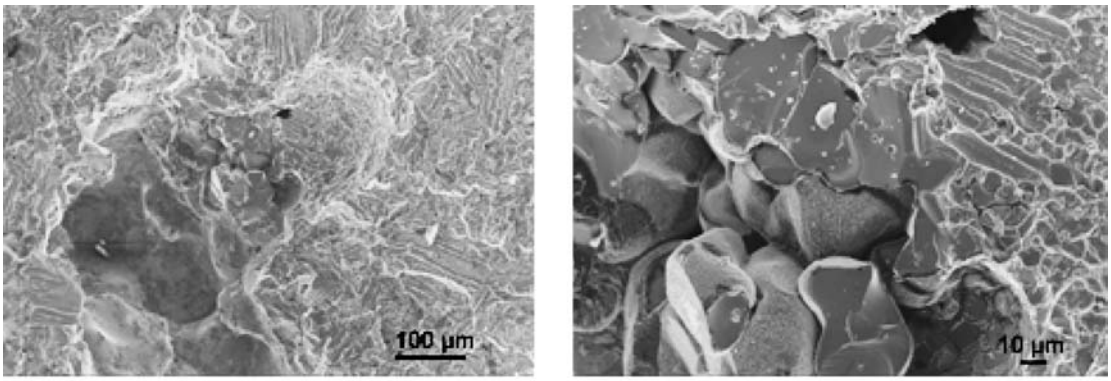

Figure 7 Fracture surface of a powder A sample (sintered 1270°C, 5 h in Ar-flow, heat treated), (a) overview, (b) detail of defects. Predominantly brittle fracture mode is obvious.

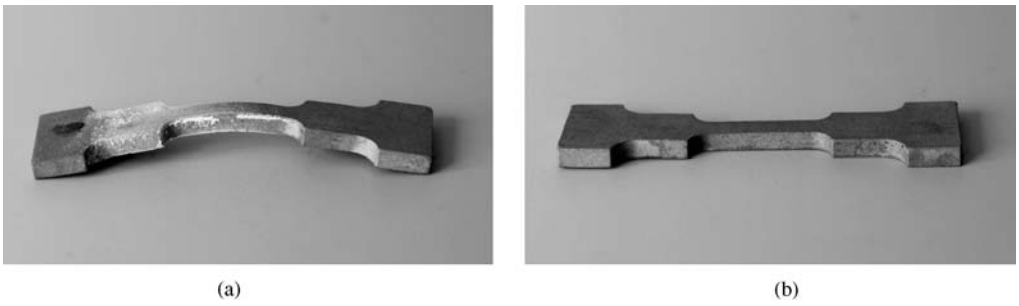

Figure 8 Demonstration of the 1WE for a powder B specimen. (a) cooled and deformed, (b) reheated with complete shape recovery.

the microstructure of MIM specimens will be made. Considering the low fracture strain, loading/unloading experiments were performed with up to 1% strain. A small hysteresis and a full strain recovery is observed (Fig. 6B).

The fracture surface shows mainly ductile regions with some large defects (Figs 7a and b). In detail, cavities can be determined obviously caused by disruption of particles. A fine-grained structure, likely oxides, is visible. Weak bonded particles of about 50 μm in diameter also covered with a fine granular layer are observed.

It can thus be assumed that the formation of second phases leads to microstructural inhomogeneities responsible for the low fracture strain of the MIM specimens. Therefore, further investigations have to focus on reducing the oxygen content, for example by the use of reducing sintering atmospheres, suitable sintering additives and further improvement of the debinding process.

Specimens from powder *B* sintered at 1250°C for 10 h in vacuum were tested at three different temperatures. The first temperature of 70°C is higher than A_f (68°C). The maximum strain obtained is 3.8% with a fracture strain of 2.9% (Fig. 6C). A nearly full strain recovery indicating pseudoelastic behaviour is observed when cycling a sample with a constant loading/unloading rate of 0.5 mm min^{-1} but at a temperature between A_p and A_f, where the martensite→austenite transformation is not complete. By heating the sample above A_f, the shape recovery is complete.

Samples tested at room temperature in a mixed pseudoelastic/pseudoplastic state show the expected lower stress of 315 MPa necessary for the martensite plateau (Fig. 6d). The yield maximum strain is 5.1% with a fracture strain of 3.8%. A slight increase in the stress strain curves indicates the start of the third region where the oriented martensite is deformed elastically.

The one-way effect is demonstrated using a tensile test specimen but loading it under a three-point bending condition. The maximal pseudoplastic deformation (bending approx. 5 mm) can be seen in Fig. 8a. The sample, deformed in the martensitic state, shows shape recovery when heated to temperatures of about A_s (Fig. 8b).

To demonstrate the functionality of MIM samples exploiting the one-way effect, hollow cylinder specimens prepared from powder *B* were cooled down to about −30°C and expanded with a mandrel by 0.7 mm (7%) in diameter without any obvious damage. Two tubes were connected by the cylinder when shape recovery took place by reheating the specimen (Fig. 9).

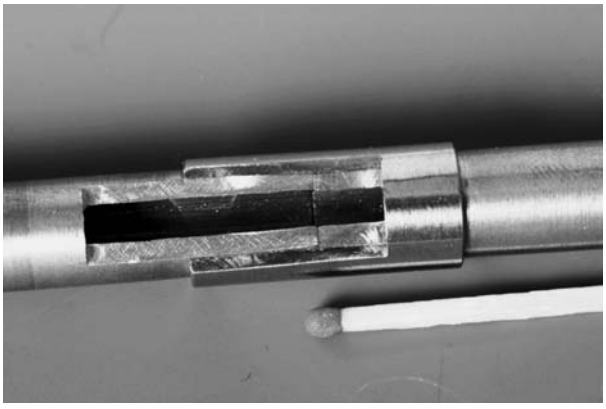

Figure 9 Two tubes connected with a coupling element prepared from the hollow cylinder.

4. Conclusions

Metal injection molding (MIM), a powder metallurgical method commonly used to produce near-net-shape parts from alloys such as steel or bronze, was applied for NiTi shape-memory alloys. Tensile test specimens for examining mechanical properties and also hollow cylinders as fitting elements were prepared from pre-alloyed NiTi powder. Though a sintering temperature near the melting point was necessary to reach sufficient densities with closed porosity. High accuracy and good dimensional stability of the specimens was obtained. After an appropriate heat treatment, well-defined martensite ↔ austenite transformations were observed. In the tensile tests, a maximum strain at failure of 5% was determined. Also the demonstration of pseudoelasticity and pseudoplasticity (one-way effect) on model parts provided promising results for applying the MIM process for shape-memory alloys. Nevertheless, oxide phases remaining from the MIM process are observed as second phases in the bulk, and were identified as the starting point for failure. Therefore, further attempts to reduce these phases have to be made, for example by the optimization of sintering conditions. Also the investigation of the fatigue behavior is an important aspect for future research.

Acknowledgements

This work is financially supported by the Deutsche Forschungsgemeinschaft (DFG) as part of the Sonderforschungsbereich SFB 459 (Formgedächtnistechnik) of the Ruhr-Universität Bochum.

References

1. E. HORNBOGEN, *Metall* **41** (1987) 488.
2. H. FUNAKUBO, in "Shape memory alloys", (Gordon and Breach Science Publishers, New York, 1987) p. 200.
3. J. VAN HUMBEECK, R. STALMANS and P. A. BESSELINK in "Metals as Biomaterials", edited by J. A. Helsen, H. J. Breme, (John Wiley & Sons, Chichester, 1998) p. 73.
4. L. BATAILLAD, J. -E. DIDAUX and R. GOTTHARDT, *Phil. Mag. A* **78** (1998) 327.
5. J. KHALIL-ALLAFI, X. REN and G. EGGELER, *Acta Mater.* **50** (2002) 793.
6. W. TANG, B. SUNDMAN, R. SANDSTRÖM and C. QUI, *ibid.* **47** (1999) 3457.
7. A. ISHIDA, M. SATO, A. TAKEI, K. NOMURA and S. MIYAZAKI, *Metall. Mater. Trans.* **27A** (1996) 3753.
8. K. GALL, K. JUNTUNEN, H. J. MAIER, H. SEHITOGLU and Y. I. CHUMLYAKOF, *Acta Mater.* **49** (2001) 3205.
9. Y. SHUGO, S. HANADA and T. HONMA, *Bull. Res. Inst. Min. Dress. Metall. Tohuku Univ.* **41** (1985) 35.
10. T. HONMA, in "Shape memory alloys", edited by H. Funakubo, (Gordon and Breach Science Publishers, New York, 1987) p. 61.
11. P. OLIER, F. BARCELO, J. L. BECHADE, J. C. BRACHET, E. LEFEVRE and G. GUENIN, *J. Phys. IV France* **7** (1997) C5-143.
12. S. K. WU, H. C. LIN and C. C. CHEN, *Mat. Letters* **40** (1999) 27.
13. H. KATO, T. KOYARI, M. TOKIZANE and S. MIURA, *Acta metall. Mater.* **42** (1994) 1351.
14. M. D. MCNEESE, D. C. LAGOUDAS and T. C. POLLOCK, *Mater. Sci. Eng.* **A280** (2002) 334.
15. M. BRAM, A. AHMAND-KHANLOU, A. HECKMANN, B. FUCHS, H. P. BUCHKREMER and D. STÖVER, *Mater. Sci. Eng.* **A337** (2002) 254.
16. R. M. GERMAN, Powder Injection Molding, Metal Powder Industries Federation, Princeton, (1990).
17. J. W. NEWKIRK, J. A. SAGO and G. M. BRASEL, in Processing and Fabrication of Advanced Materials VII, edited by T. S. Srivatsan and K. A. Khor, The Minerals, Metals and Materials Society, Warrendale, (1998) 213.
18. H. KYOGOKU and S. KOMATSU, *J. Jap. Soc. Powder and Powder Metallurgy* **46** (1999) 1103.
19. B. Y. LI, L. J. RONG., Y. Y. LI and V. E. GJUNTER, *Acta Mater.* **48** (2000) 3895.
20. S. M. GREEN, D. M. GRANT and N. R. KELLY, *Powder Metall.* **40** (1997) 43.
21. C. M. CHANG, S. TRIGWELL and T. DUERIG, *Surf. Interf. Anal.* **15** (1990) 349.
22. C. L. CHU, S. K. WU and Y. C. YEN, *Mater. Sci. Eng. A* **216** (1996) 193.
23. W. XIAOXIANG, *Trans. Nonferrous Met. Soc. China* **8** (1998) 455.
24. D. TREPPMANN, Thermomechanische Behandlung von NiTi, Fortschrittsberichte VDI, VDI Verlag Dortmund (1997).
25. X. REN, N. MIURA, J. ZHANG, K. OTSUKA, K. TANAKA, M. KOIWA, T. SUZUKI, Y. I. CHUMLYAKOV and M. ASAI, *Mater. Sci. Eng. A* **312** (2001) 196.
26. J. KHALIL-ALLAFI, A. DLOUHY and G. EGGELER, *Acta Mater.* **50** (2002) 4255.
27. E. SCHÜLLER, M. BRAM, O. A. HAMED, D. SEBOLD, H. P. BUCHKREMER and D. STÖVER, to be published, *Adv. Eng. Mat.*

Received 25 March 2004
and accepted 11 March 2005